Chemosphere 358 (2024) 142140

Contents lists available at ScienceDirect

Chemosphere

journal homepage: www.elsevier.com/locate/chemosphere

Exceptional performance of Fe@carbon-rich nanoparticles prepared via hydrothermal carbonization of oil mill wastes for H_2S removal

M. Abid [a], R. Garcia [b], M. Martinez-Escandell [a], A. Fullana [b], J. Silvestre-Albero [a,*]

[a] Laboratorio de Materiales Avanzados, Departamento de Química Inorgánica-Instituto Universitario de Materiales, Universidad de Alicante, Spain
[b] Departamento de Ingeniería Química, Universidad de Alicante, Spain

HIGHLIGHTS

- Oil mill wastewater has been transformed into added value catalysts for H2S removal.
- Well-designed Fe-based core-shell nanoparticles have been successfully prepared.
- These composites exhibit an exceptional performance for H2S removal.

GRAPHICAL ABSTRACT

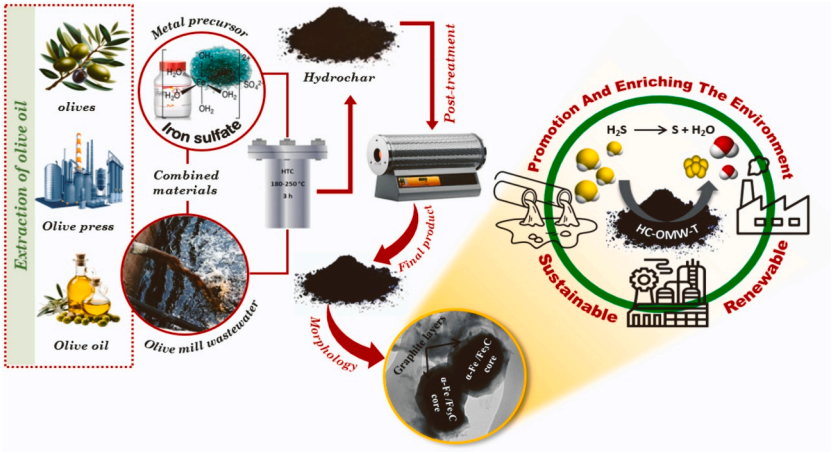

ARTICLE INFO

Handling Editor: Grzegorz Lisak

Keywords:
Hydrothermal carbonization
Core-shell nanoparticles
Fe@C
H_2S

ABSTRACT

Carbon-encapsulated iron oxide nanoparticles (CE-nFe) have been obtained from an industrial waste (oil mill wastewater-OMW, as a carbonaceous source), and using iron sulfate as metallic precursor. In an initial step, the hydrochar obtained has been thermally activated under an inert atmosphere at three different temperatures (600 °C, 800 °C and 1000 °C). The thermal treatment promotes the development of core-shell nanoparticles, with an inner core of α-Fe/Fe_3O_4, surrounded by a well-defined graphite shell. Temperatures above 800 °C are needed to promote the graphitization of the carbonaceous species, a process promoted by iron nanoparticles through the dissolution, diffusion and growth of the carbon nanostructures on the outer shell. Breakthrough column tests show that CE-nFe exhibit an exceptional performance for H_2S removal with a breakthrough capacity larger than 0.5–0.6 g $H_2S/g_{catalyst}$ after 3 days experiment. Experimental results anticipate the crucial role of humidity and oxygen in the adsorption/catalytic performance. Compared to some commercial samples, these results constitute a three-fold increase in the catalytic performance under similar experimental conditions.

* Corresponding author.
E-mail address: joaquin.silvestre@ua.es (J. Silvestre-Albero).

https://doi.org/10.1016/j.chemosphere.2024.142140
Received 9 January 2024; Received in revised form 16 April 2024; Accepted 24 April 2024
Available online 28 April 2024

1. Introduction

Hydrogen sulfide is a colorless gas with a characteristic "rotten egg" odor that is soluble in a number of liquids (e.g., water, alcohols, amines, etc.). In the atmosphere, hydrogen sulfide can undergo a number of oxidation reactions to produce sulfur dioxide and sulfuric acid, responsible for acid rain, or elemental sulfur. H_2S emissions to the atmosphere are attributed to the volcanic activity on Earth and to the degradation of plants and animal proteins by bacterial action. Industrially, H_2S is a by-product in several reaction processes (e.g., coke production from sulfur-containing coal, manufacture of viscose rayon, pulp and paper processing, etc.), and it is also an important reagent in some processes. H_2S is also a typical impurity in fuel gases, such as natural gas, biogas, syngas, etc., and wastewater streams. The World Health Organization (WHO) and the National Institute for Occupational Safety and Health (NIOSH) have defined an occupational exposure limit for H_2S of 10–15 mg/m^3 (7–10 ppm) in an 8h time-weighted-average or a ceiling limit of 20 ppm in workplace air for a 15-min time-weight-average (WHO Report, 1981; EPA Report, 2016). These stringent regulations require the design of novel, cost-effective technologies for the efficient capture and removal of H_2S from industrial streams (Pudi et al., 2022; Sun et al., 2022). In addition to the toxic effects identified, ppm levels of H_2S in industrial streams can cause severe problems due to the corrosion of pipes, equipments, as well as poison downstream catalysts. Among the different possibilities to remove hydrogen sulfide (amine scrubbing, biofilters, etc.), adsorption in the cavities of nanoporous solids (e.g., using carbon materials) can be considered a promising approach for industry owing to its affordability, flexibility, energy efficiency, and ease of operation (Liu et al., 2020). In a very comprehensive study, Bandosz et al. identified the critical aspects defining the performance of activated carbon materials for H_2S adsorption/oxidation (Bandosz et al., 2002). Parameters such as pore size (smaller pores can be important for the process), surface chemistry, presence of water, surface pH, etc., were identified as critical parameters defining the adsorption/oxidation capacity and the selectivity towards the final products. Activated carbons' performance for hydrogen sulfide removal can be highly improved by surface impregnation with caustic substances, e.g., NaOH, KI, or KOH (Bandosz et al., 1999; Bagreev and Bandosz, 2022). However, impregnation with these chemicals has several disadvantages such a decrease in the ignition temperature of the carbon, corrosion problems, production of elemental sulfur as the main reaction product, etc. Incorporation of metal species in the carbon material has been also proposed as a promising approach to enhance the oxidation performance towards H_2S. Impregnation with transition metal salts (e.g., iron, copper, zinc, etc.) has been described in the literature to enhance the catalytic performance of carbon materials with a small additional cost (Chen et al., 2022; Balsamo et al., 2016; Choudhury and Lansing, 2021). One of the critical aspects in the preparation of metal/carbon composites concerns the presence of a highly dispersed active phase, with an optimum in the number of exposed active sites, and the mitigation of potential sintering phenomena. A promising approach to achieve highly dispersed metal oxide nanoparticles in a carbon matrix consists in the catalytically assisted hydrothermal carbonization (HTC) of organic precursors. This approach allows to fabricate metal/carbon nanoarchitectures (Te, Fe, etc.) under mild synthesis conditions, with controlled size and shape, in most cases, with a core-shell morphology, and more importantly, with the possibility to use biomass-residues as carbon source (Qian et al., 2006; Yu et al., 2004; Calderón et al., 2018; Muñoz et al., 2021; Vargas-Estrada et al., 2023).

Taking into account the promising results achieved so far with HTC to reach highly dispersed metal nanoparticles, the main goal of this manuscript is the synthesis, characterization and application of iron oxide nanoparticles encapsulated in carbon-rich nanostructures obtained via a one-pot synthesis approach through hydrothermal metal-catalyzed carbonization (HTC). A biomass residue from the oil processing industry (Alpechin) was used as a carbon source. The synthesized hybrid nanoparticles have been characterized using a number of techniques and their catalytic performance has been tested in the dry/humid removal of H_2S in industrial simulated streams.

2. Materials and methods

2.1. Synthesis of metal-doped hydrochars

The nanoparticles used were synthesized at the spin-off company CALPECH (Ce-in Plus) belonging to the University of Alicante. These consist of iron oxide nanoparticles covered by an amorphous carbonaceous layer. The nanoparticles were synthesized from olive mill wastewater (known as Alphechin) through a hydrothermal carbonization process (HC-OMW), similar to the ones described elsewhere, but using $FeSO_4$ as a metal precursor (Calderón et al., 2018). Once synthesized, iron nanoparticles were thermally treated or "activated" at high temperatures in a horizontal furnace. Briefly, the HC-OMW sample was spread in an alumina boat and thermally treated at the desired temperature (600–1000 °C) for 3h under a nitrogen flow (100 ml/min; heating ramp: 10 °C/min). Upon completion of the thermal treatment, samples were cooled down and exposed to water vapour in the temperature range from 100 °C down to room temperature. The passivation step using humid nitrogen is mandatory to avoid ignition upon air exposure. The obtained products were labelled HC-OMW-T, where T represents the activation temperature.

2.2. Sample characterization

Phase composition of the evaluated samples was identified using XRD. These analyses were performed in a Bruker diffractometer (model D8-Advance) equipped with a copper anode and a Goebel mirror. Textural properties were evaluated through nitrogen adsorption at cryogenic temperatures (−196 °C) using a home-built manometric equipment designed and constructed by the "Laboratorio de Materiales Avanzados" group (and now commercialized by Gas-to-Materials – www.g2mtech.com). Before gas adsorption measurements, samples were outgassed at 250 °C for 4h. The surface area was calculated using the BET method, while Dubinin-Radushkevich equation was applied to estimate the micropore volume. Raman spectroscopy studies were performed using a Jasco NRS-5100 spectrometer working with a laser of 532 nm and a CCD detector.

X-ray photoelectron spectroscopy (XPS) analyses were performed using a K-ALPHA Thermo Scientific instrument (pressure 5×10^{-7} N m^{-2}). The spectra were collected using Al–K radiation (1486.6 eV) with a twin crystal monochromator, generating a focused X-ray spot with a diameter of 400 nm, at 3 mA × 12 kV.

Transmission electron microscopy (TEM) measurements were obtained using a TEM 120 kV JEOL JEM-1400Plus model equipped with an image acquisition camera GATAN model ORIUS with a resolution of 0.38 nm between points and 0.2 nm between lines. The morphology of the synthesized carbon materials was evaluated using field-emission scanning electron microscopy (FESEM). These analyses were collected in a Merlin VP Compact system from ZEISS equipped with an EDX microanalyzer Quantax 400 from Bruker with a resolution of 0.8 nm at 15 kV and 1.6 nm at 1 kV.

Thermogravimetric analyses were carried out in a Mettler Toledo TG-DSC2 equipment using 20 mg of sample in an alumina crucible and a thermal treatment up to 1500 °C in air or nitrogen, accordingly (100 ml/min; heating rate 10 °C/min).

2.3. Breakthrough tests

H_2S breakthrough column experiments were performed in a fixed bed tubular reactor (i.d. 1 cm and height 15 cm) at room temperature using *ca.* 0.5–1 g of sample. A total flow of 80 ml/min was used (space velocity ≈ 2000-3000 h^{-1}) by combining two different gas cylinders, i.e.

40 ml/min of mixture (I) containing H_2S (1600 ppm)/N_2 (50%)/CO_2(50%), and 40 ml/min of a mixture (II) containing N_2/O_2 (5% O_2). H_2S concentration was continuously monitored using an electrochemical detector from Dräguer. The inlet concentration was always fixed at 800 ppm and breakthrough tests were stopped after 72h. Moisture was added using a glass saturator (relative humidity range 40–70%).

3. Results and discussion

3.1. Synthesis and characterization of the core-shell nanoparticles

Understanding the conversion of biomass-derived residues into advanced hydrochars is challenging due to the complexity of the reaction processes taking place under hydrothermal carbonization conditions (HTC) (Shi et al., 2019). In a first step, cellulose and hemicellulose in the biomass are hydrolyzed to biomolecules, such as lipids, tannins, glucosides, carbohydrates, etc., and subsequently converted (e.g., aldol condensation) into polyphenols, amino acids, aldehydes, and peptides. In a subsequent step, these primary key components are oxidized (e.g., quinones) and polymerized to more complex structures, including humid macromolecules (Wei et al., 2022). The final product, hydrochar, is a solid polymer rich in unsaturated polycyclic structures and a rich surface chemistry (oxygen functional groups) (van Zandvoort et al., 2015; Sevilla and Fuertes, 2009). Previous studies described in the literature have anticipated that alphechin-based residues (coming from the olive oil extraction process), modified with iron salts, can be converted into well-defined zero-valent iron nanoparticles (CE-nFe) with core-shell morphology via hydrothermal carbonization (Calderón et al., 2018; Muñoz et al., 2021; Vargas-Estrada et al., 2023). Under hydrothermal conditions, iron nanoparticles are encapsulated by chelating agents (e.g., polyphenols), and after polymerization/aromatization give rise to a brownish solid made of carbon nanostructures encapsulating iron nanoparticles. One of the open questions at this stage is the amount and nature of these iron nanoparticles and the structure and morphology of the carbon layers. To this end, several characterization techniques have been applied to the CE-nFe sample. Fig. S1 shows the thermogravimetric (TG) analysis in an air atmosphere of the original sample (called HC-OMW). TG profile shows several weight losses in the temperature range 200–600 °C, the main contribution at 210 °C (*ca.* 40%) due to the combustion of amorphous carbon encapsulating the iron nanoparticles. Upon complete combustion, the remaining metal content is 41.6 wt%.

Hydrothermally synthesized hydrochars do not exhibit porosity and a thermal processing or "activation treatment" is needed. This activation is performed under an inert atmosphere (e.g., N_2) and gives rise to a highly porous network through the conversion of the amorphous carbon-based precursors into ordered graphite and/or graphene microdomains. This re-structuring process must be assisted by iron nanoparticles, thus explaining the core-shell morphology observed (Fig. 1A). TEM images confirm the core-shell morphology with well-defined carbon layers encapsulating iron nanoparticles. Interestingly, the width of the carbon shell increases with the activation temperature (from ca. 10 nm at 600 °C to ca. 50 nm at 1000 °C). A careful evaluation of these shells allows to identify some structural ordering in the form of graphene/graphite layers. The observed morphology and the identification

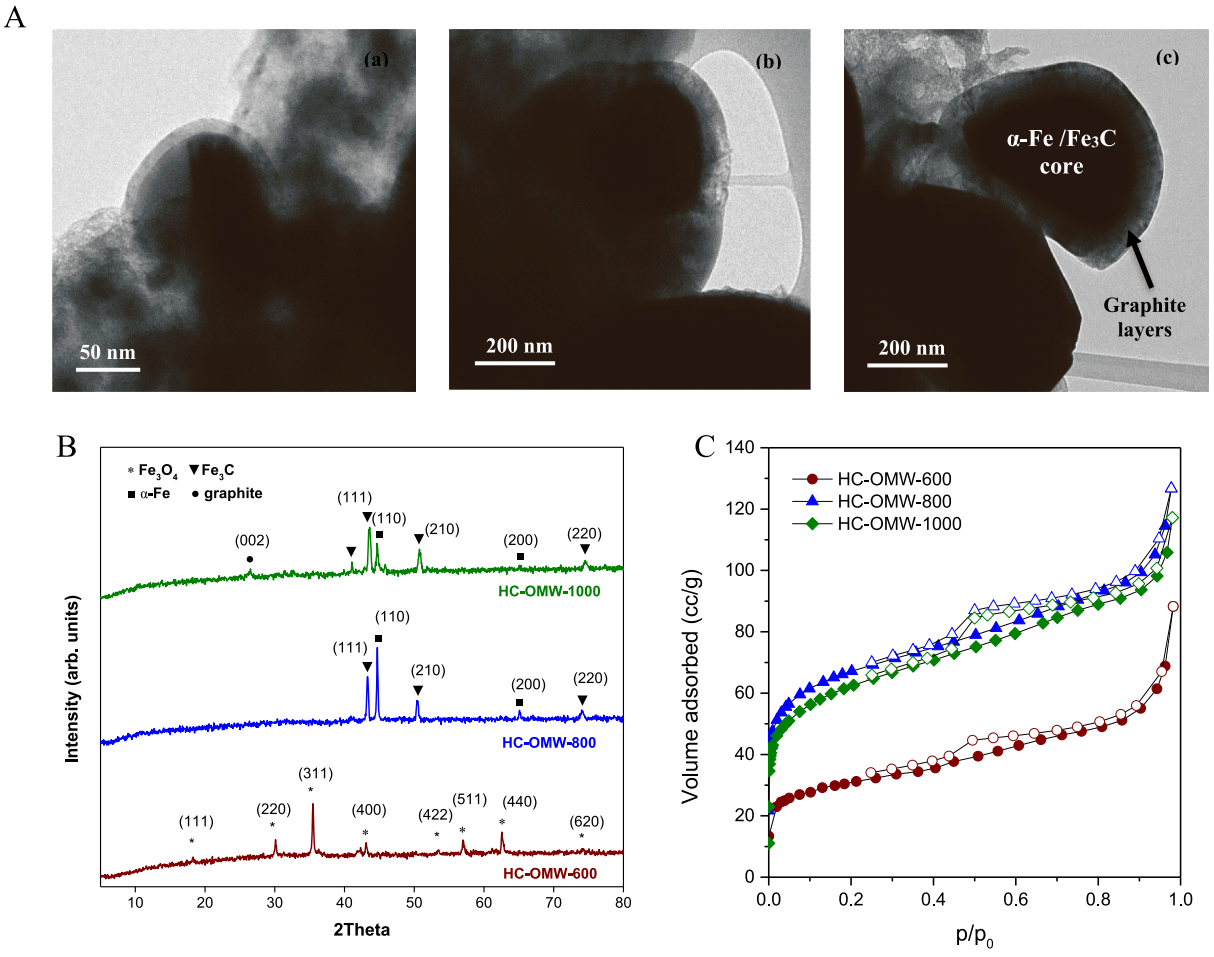

Fig. 1. **A** TEM images for (a) HC-OMW-600, (b) HC-OMW-800 and (d) HC-OMW-1000, **B** XRD pattern for the different samples after the activation step, **C** Nitrogen adsorption/desorption isotherms for the activated samples.

of Fe_3C species (Fig. 1 A&B) provide some light into the formation mechanism, most probably through the dissolution of amorphous carbon species in the iron nanoparticles and their subsequent reorganization in the outer shell, similar to the growth of carbon nanotubes on Fe or Co nanoparticles. This mechanism involves the decomposition of the carbon precursors, diffusion of carbon into the iron nanoparticles (through the formation of iron carbide) and the restructuring of these carbon nanostructures at the interface (Abdullah et al., 2017). For large metal nanoparticles (>50 nm, such as the ones used in this study), nanoonions are favored over carbon nanotubes (Gore and Sane, 2011). XRD pattern of the activated samples reflects a significant difference in composition for the iron nanoparticles, depending on the activation temperature applied. At low temperatures (e.g., 600 °C), Fe_3O_4 is the main phase. Higher temperatures (above 800 °C) are needed to identify the presence of iron carbide, metallic iron (α-Fe) and graphite. In other words, temperatures above 800 °C are needed to promote the nanoonions growth mechanism. TEM images suggest that although these ordered graphite nanostructures are already formed at 600 °C, their width is larger at 800 °C and above. TEM images also anticipate the presence of larger iron nanoparticles (metal sintering) for sample HC-OMW-1000. Nitrogen adsorption/desorption isotherms (Fig. 1C) confirm the development of the porosity with the activation temperature (preferentially above 800 °C). The BET surface area scales from 110 m^2/g, for sample HC-OMW-600, up to a maximum around 230–245 m^2/g, for samples activated at 800 °C and 1000 °C (Table S1). These results confirm that carbon deposits surrounding iron nanoparticles are porous, the newly developed micro- and mesopores being responsible for the increased surface area. Nitrogen adsorption data confirm the presence of a widely developed microporous structure (rounded knee at low relative pressures), together with well-defined mesocavities. Furthermore, mesoporosity is evident in all samples due to the presence of a market hysteresis loop down to $p/p_0 \approx 0.42$ (Type H4, according to the IUPAC), attributed to mesopores of *ca.* 4–6 nm (Fig. S2) (Thommes et al., 2015). Fig. S3 shows the Raman spectra for the three evaluated hydrochar samples. The sample activated at low temperatures (HC-OMW-600) exhibits a rather flat spectrum due to the amorphous nature of the carbon deposits on the iron nanoparticles. The scenario changes drastically for samples thermally treated at higher temperatures. For these samples (800 °C and above), the Raman spectra consist of two well-defined overlapping bands at around 1332 cm^{-1} and 1573 cm^{-1}, known as D (assigned to ring-breathing vibrations in benzene or condensed benzene rings) and G (assigned to in-plane bond--stretching motion of pairs of C sp^2 atoms in aromatic and olefinic molecules) bands, respectively, characteristic of carbonized materials (Cuesta et al., 1994). These results anticipate that aromatization/-graphitization of the hydrochars takes place after a high-temperature thermal treatment, in close agreement with XRD observations and N_2 adsorption isotherms. Evaluation of the I_D/I_G ratio shows that this ratio increases for sample HC-OMW-1000, i.e., graphitization is higher at high temperatures. Furthermore, Raman spectra for this sample reflects a contribution at 2674 cm^{-1} (second order of zone-boundary phonons), attributed to the 2D band of graphene/graphite layers (Ferrari et al., 2006). Interestingly, the asymmetry of the 2D band at low Raman shifts and the lower intensity of the 2D band compared to the G band suggests the preferential formation of defective graphite microdomains, in agreement with XRD results.

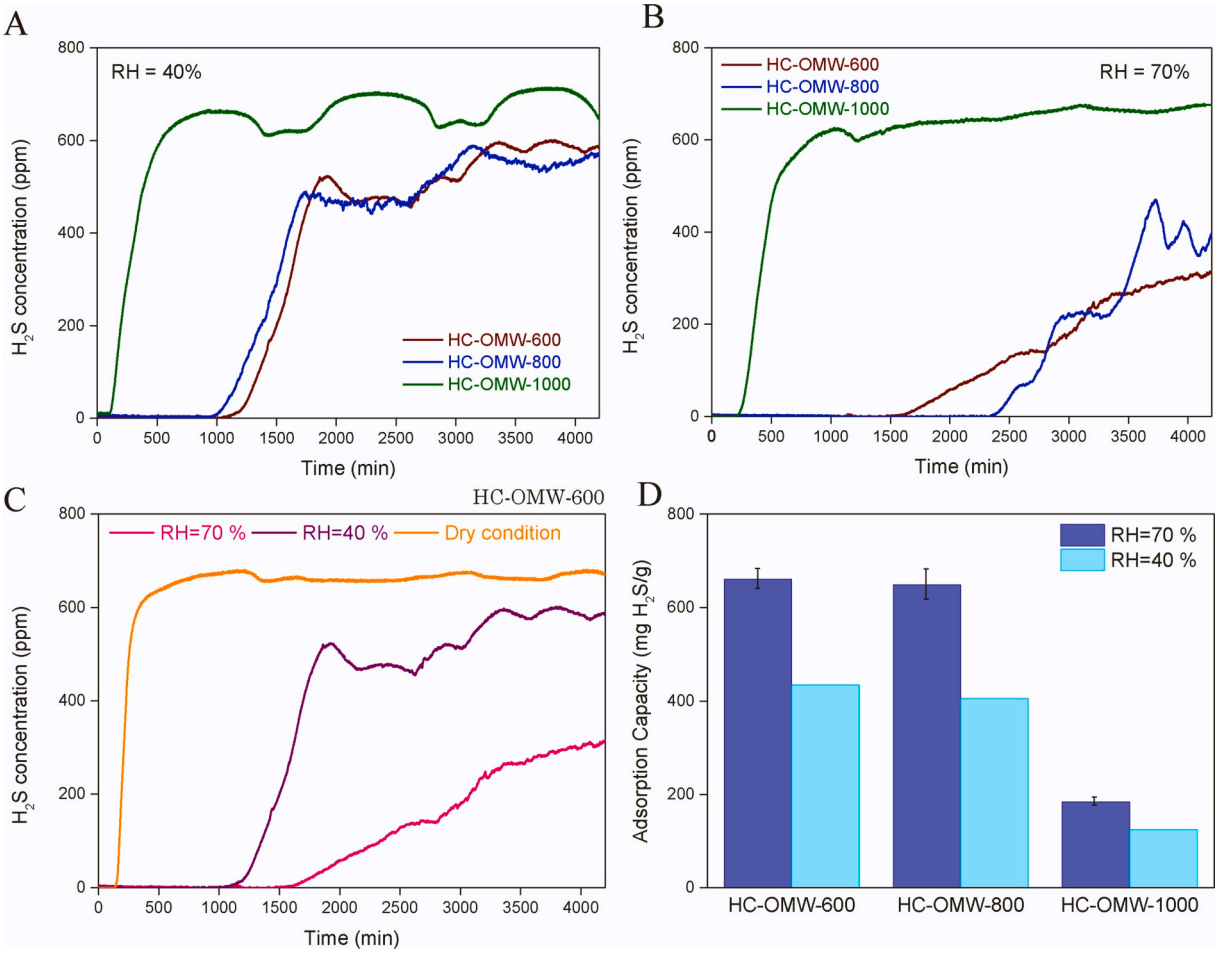

Fig. 2. A & B H_2S breakthrough column experiments at 25 °C for the different samples evaluated at two different humidity ratios (40 and 70%); **C** Effect of the humidity for sample HC-OMW-600 and **D** Summary of the adsorption/catalytic performance for all samples.

3.2. Catalytic performance of the Fe-based nanoparticles

The catalytic performance of the synthesized nanoparticles has been tested in the removal of H_2S at low concentrations (800 ppm) and room temperature. Fig. 2 A&B shows the breakthrough column experiments at two different humidity ratios (40 and 70%). In both scenarios, the catalytic performance follows a similar tendency, i.e., samples HC-OMW-600 and HC-OMW-800 exhibit an exceptional performance, while sample HC-OMW-1000 breaks down relatively fast (at this point it is important to highlight that temperatures below 600 °C were tested but with poor adsorption/catalytic performance). Furthermore, these results anticipate a promoting effect of humidity for all samples, the adsorption/catalytic performance being highly improved for the samples tested under 70% relative humidity. The crucial role of H_2O in the catalytic process can be more clearly discerned in Fig. 2C. Sample HC-OMW-600 exhibits a poor performance under dry conditions (114 mg/g), with a breakthrough time of *ca.* 153 min. Incorporation of 40% relative humidity improves the catalytic performance (removal capacity 434 mg/g), with a breakthrough time of *ca.* 1216 min, and finally, the sample tested at 70% relative humidity exhibits a removal performance as high as 661 mg/g, with a total break time of *ca.* 1650 min. These results are summarized in Fig. 2D and Table S2. Overall, breakthrough tests reflect the exceptional performance of samples HC-OMW-600 and HC-OMW-800 at high humidity ratios (*ca.* 650–660 mg/g for both samples). At this point, it is important to highlight that the non-activated sample (HC-OMW) exhibits a total removal capacity of *ca.* 2 mg/g (not shown), i.e., the thermal processing step at 600 °C and above is crucial in the development of the active sites for the catalytic conversion of H_2S. The activation step also promotes the development of the porosity, although the effect of the porosity in the H_2S removal process, if any, must be minimal considering the drastically different performance of samples HC-OMW-800 and HC-OMW-1000 (despite a similar porosity). The crucial role of water in the oxidation mechanism has been widely described in the literature (Kaliva et al., 1983). In fact, H_2O is needed in the initial steps of the reaction to promote H_2S dissolution and dissociation to hydrogen sulfide ions (HS^-) and the formation of iron hydroxides.

To check the reproducibility of the synthesis procedure, samples HC-OMW-T have been reproduced using the original HC-OMW residue and following the activation procedure described above. Reproduced samples (batch 2) have been tested in the H_2S adsorption process exclusively at 70% relative humidity and 25 °C. As it can be appreciated in Fig. S4, the breakthrough profiles for batch 2 are rather similar to those obtained with batch 1, for the three samples evaluated. The results obtained with samples HC-OMW-600 and HC-OMW-800 are exceptional, with values above 550–600 mg/g. However, these numbers are slightly lower than those obtained in the first batch, preferentially for sample HC-OMW-800 (i.e., 649 vs 564 mg/g – 13% lower). The larger difference for the sample activated at 800 °C (only 7% in the case of sample HC-OMW-600) demonstrates that highly activated samples are more heterogeneous in nature and the reproducibility has larger variance. A third batch was produced (not shown) to estimate the uncertainty for H_2S removal depending on the sample evaluated. Total adsorption values were 632 ± 24 mg/g (HC-OMW-600), 607 ± 42 mg/g (HC-OMW-800) and 188 ± 4 mg/g (HC-OMW-1000). Furthermore, samples HC-OMW-T (batch 1) were evaluated 6 months after preparation to identify potential aging processes. Fig. S5 shows that the breakthrough profiles keep the original shape after aging, although the adsorption performance slightly decreases for all samples (ca. 15–25%). In any case, the obtained results for samples HC-OMW-600 and HC-OMW-800 are always close to or above 500 mg/g, independently of the batch evaluated and the aging process, thus confirming the exceptional quality of these samples for H_2S removal.

Another key component in the catalytic tests is the presence of oxygen in the reaction mixture. As described in the experimental section, the results described in Fig. 2 were performed with 2.5% of O_2 in the gas mixture. To identify the crucial role of oxygen in the catalytic process, similar experiments were performed for sample HC-OMW-600, but using pure nitrogen instead of a N_2/O_2 mixture. Breakthrough column experiments in Fig. S6 demonstrate the drastic effect in the reaction process after the incorporation of a small oxygen content (2.5%). In the absence of oxygen, the catalytic performance is significantly decreased with a total capacity as low as *ca.* 61 mg/g. In summary, breakthrough column experiments demonstrate that CE-nFe nanoparticles activated at temperatures between 600 °C and 800 °C are exceptional materials for the removal of H_2S in industrial streams, preferentially in the presence of oxygen and humidity.

To complete the catalytic/adsorption evaluation, a final test was performed to evaluate the potential regeneration of these catalysts after the H_2S breakthrough column experiments. Two different regeneration approaches were applied to the exhausted samples (4200 min under H_2S reaction conditions): (A) a thermal treatment at 300 °C for 4h using a humid nitrogen flow (200 ml/min; heating rate 10 °C/min), or (B) a simple regeneration process flowing pure nitrogen at 25 °C overnight until no sulfur is detected in the sensor. Fig. S7 shows that none of the regeneration approaches evaluated is suitable to recover the original adsorption/catalytic activity of sample HC-OMW-600. In both cases, after 4200 min under working conditions (experiment 1) the catalysts are nearly deactivated, and only the cleaning process with nitrogen at 25 °C is able to recover partly some catalytic activity. Overall, these findings anticipate that the regeneration is a complex process and novel approaches must be evaluated in future studies.

3.3. Characterization of the used catalysts

To ascertain the nature of the active species, iron-encapsulated nanoparticles have been characterized after the H_2S experiments (labelled HC-OMW-T-af). XRD patterns of the used samples (Fig. 3A) show the characteristic contributions for Fe_3O_4, for sample HC-OMW-600, and α-Fe and Fe_3C, for samples HC-OMW-800 and HC-OMW-1000. In addition, some tinny contributions due to elemental sulfur (S_8) at 25° and 28°, and FeS can be discerned, preferentially for the most active catalysts. XPS analyses have also been used to estimate the surface composition of the different catalysts before and after the H_2S tests (Table S3). As expected, the original samples contain a high carbon (70–90 at.%) and oxygen (7–25%) content. In addition, original samples contain a significant amount of iron, and some residual sulfur due to the metal precursor used ($FeSO_4$). Iron and oxygen contents decrease for the sample activated at 1000 °C due to the decomposition of the surface functionalities and the sintering of the metal nanoparticles at high temperatures. After exposing the iron nanoparticles to H_2S, the chemical composition of the catalysts remains relatively unchanged, except the sulfur content that highly increases with a maximum for sample HC-OMW-800, in close agreement with the catalytic data. The comparison of the XPS spectra in the Fe2p region for the fresh and used catalysts is shown in Fig. 3B. XPS spectra show the characteristic peaks of Fe_3O_4 with maxima at 709.8 eV (Fe^{2+}) and 711.0–713.1 eV (Fe^{3+} octahedral and tetrahedral, respectively) (Yang et al., 2014; Li et al., 2019). These results are in close agreement with the XRD patterns described above. The absence of peaks due to iron carbide (*ca.* 708.2 eV) and metallic iron (*ca.* 706.8 eV) must be attributed to the surface sensitivity of the XPS data (Li et al., 2019; Tian et al., 2019). The XPS spectra of the used catalysts are relatively similar those obtained for the original samples with contributions at 710.1, 711.4 and 713.7 eV, characteristics of Fe_3O_4. At this point it is important to highlight that Fe–S species will nearly overlap with the Fe–O contributions, with the associated complexity to identify changes after H_2S treatment (Zhang et al., 2017). However, a tinny contribution at 708.1 eV can be appreciated for sample HC-OMW-600-af, most probably due to Fe–S. For a better evaluation of the sulfur species formed under reaction conditions, the XPS spectra in the S2p region have been evaluated for the used catalysts (Fig. 3C). The sample activated at the lowest temperature (HC-OMW-600) exhibits the

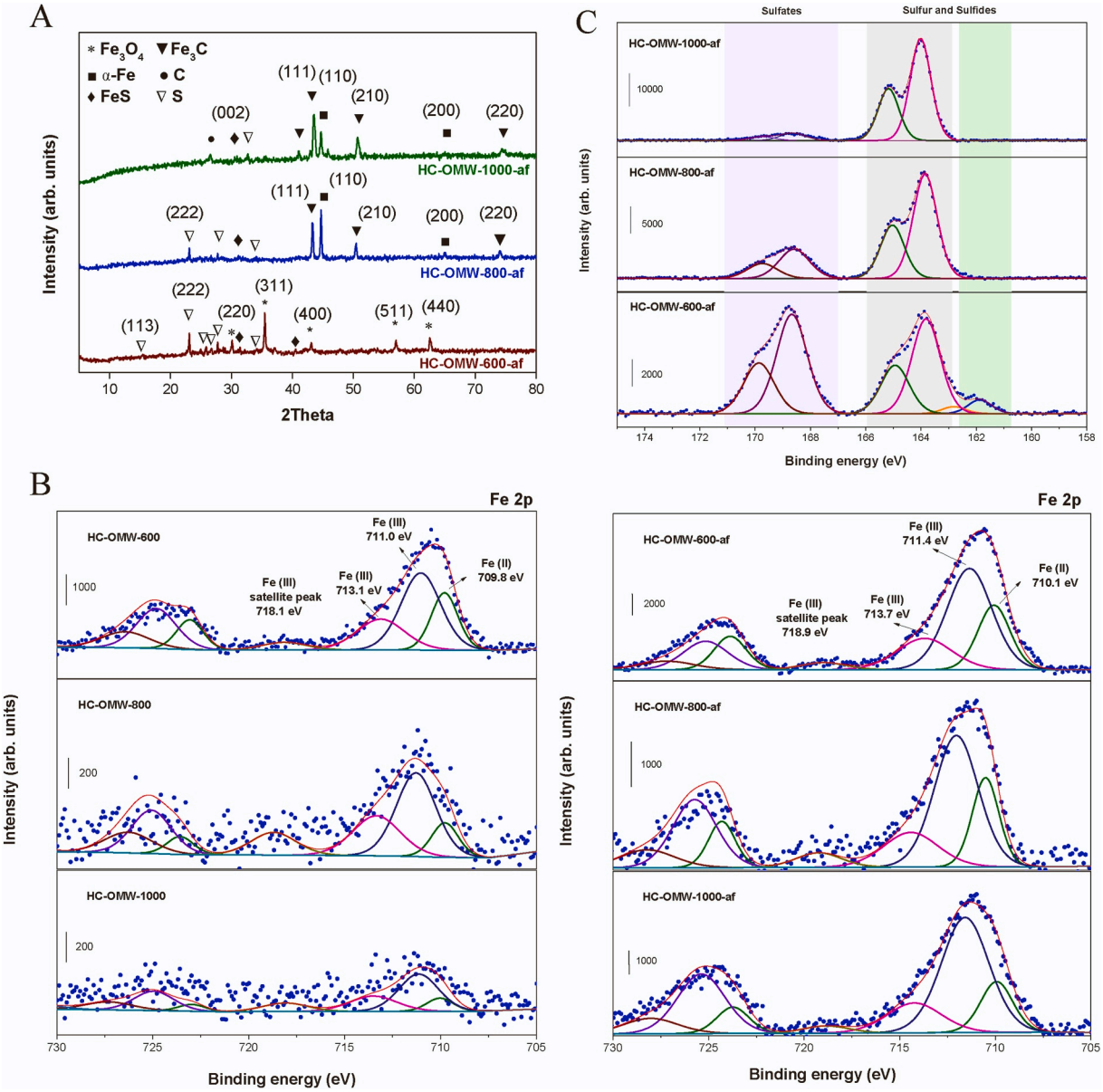

Fig. 3. **A** XRD pattern of the evaluated samples after the breakthrough tests; **B** XP spectra of the different samples in the Fe 2p region before and after the breakthrough tests, **C** XP spectra in the S2p region for the used nanoparticles.

characteristic peaks of iron sulfate (doublet at 169.8 eV and 168.6eV), sulfur and iron mono-, di- and polysulfides anions (164.9 eV, 163.8 eV, 162.8 eV and 161.9 eV). More specifically, contributions in the 165.0–161.0 eV could be assigned to elemental sulfur (164.9 eV), and sulfide anions: S_n^{2-} (163.8 eV) and S_2^{2-} and S^{2-} (162.8 eV and 161.9 eV, respectively) (Zhang et al., 2017; Lang and Butler, 2016; Mikhlin et al., 2001). Samples activated at higher temperatures (800 °C & 1000 °C) promote the formation of elemental sulfur and polysulfide anions over sulfates (coming from the metal precursor used) and mono-/disulfides. These observations will agree with the reaction mechanism described in the literature under oxygen-rich conditions, i.e., intermediate formation of sulfides (e.g., Fe_2S_3, FeS, FeS_2 and Fe_3S_4), and their subsequent oxidation to regenerate the initial oxides, and the formation of S_8 deposits or S_n^{2-} anions in carbon defects (Davydov et al., 1998; Wang et al., 2019). The in-situ regeneration of the active sites under the oxygen-rich reaction conditions applied in this study will explain the similarity in the XPS spectra for Fe, before and after H_2S tests, and the optimum performance of these HC-OMW-T catalysts for extended time-periods.

The pH of the synthesized catalysts is also an important parameter that can influence the H_2S removal capacity. Shang et al. highlighted the important role of surface pH in the adsorption performance (Mikhlin et al., 2001). Table S4 compares the pH of the original and used catalysts. Original HC-OMW sample (non-activated) exhibits a neutral pH. However, after the activation treatment, all samples exhibit an initial pH close to 10. The initial pH (highly above the pK_a for H_2S) is highly favorable for the H_2S adsorption process, although it cannot fully justify the catalytic performance (for instance, the low catalytic activity for HC-OMW-1000). In other words, although pH could define the H_2S adsorption mechanism, a basic environment is not the main factor defining the total oxidation capacity (Bandosz et al., 2002). After reaction, the pH of all samples remains basic (*ca.* 7–8), thus precluding the formation of sulfuric acid as the main reaction product in these catalysts.

The morphology of the original and used catalysts has been evaluated using FE-SEM images and mapping for C, Fe and S. Figs. 4 and 5 show representative images for the HC-OMW-600 and HC-OMW-1000 catalysts after being exposed to H_2S breakthrough column experiments. Raw images (upper left corner) show a heterogenous distribution of micrometer-size aggregates containing white spherical nanoparticles

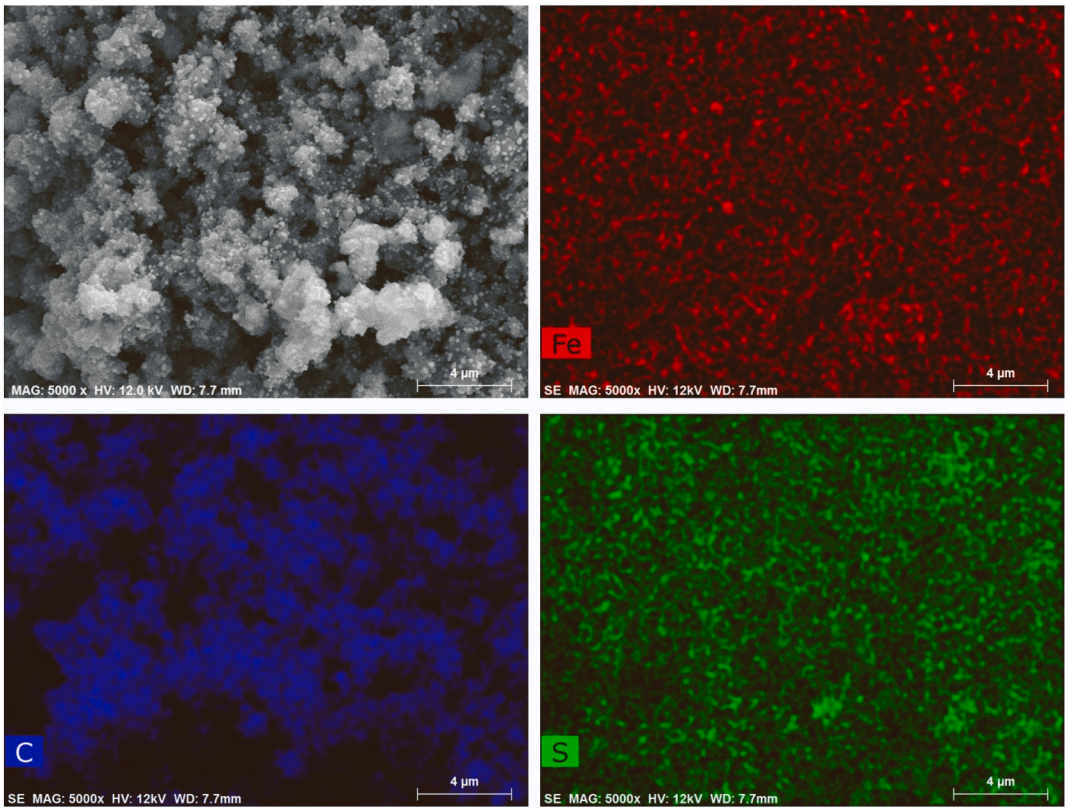

Fig. 4. FE-SEM images of the as-synthesized HC-OMW-600 sample and specific mapping for Fe, C and S.

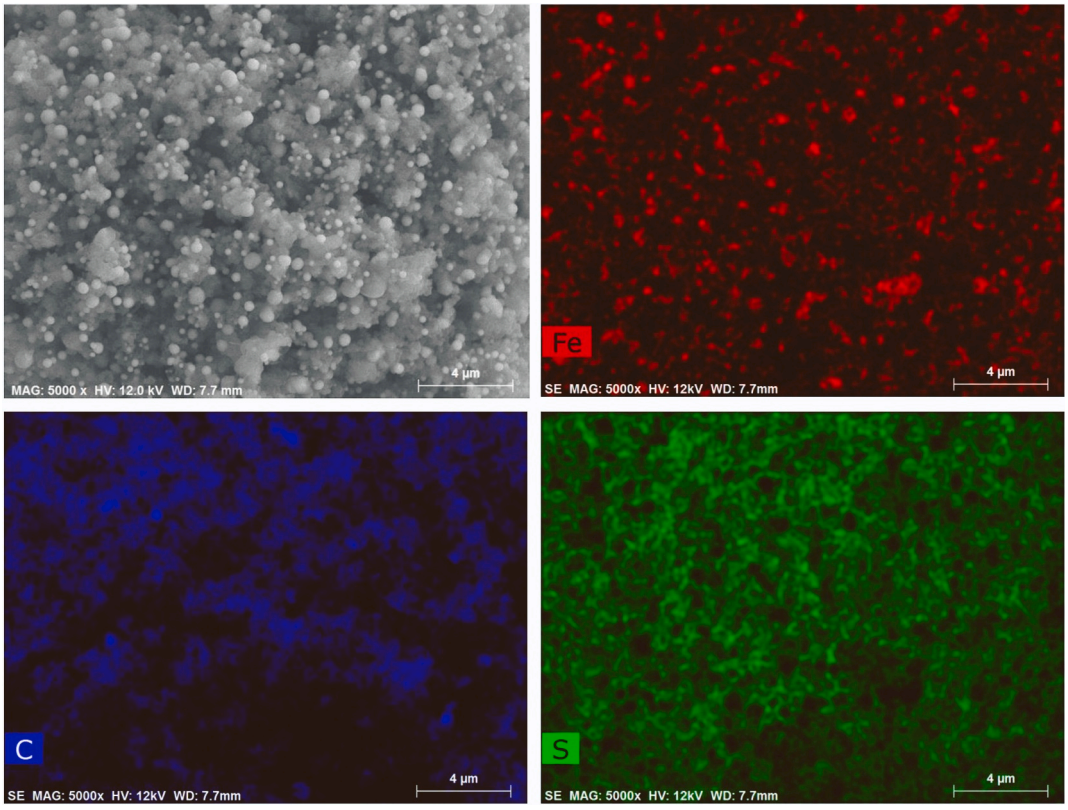

Fig. 5. FE-SEM images of the as-synthesized HC-OMW-1000 sample and specific mapping for Fe, C and S.

on the outer surface. The presence of these rounded nanoparticles on the outer surface is more clearly visible in the sample activated at 1000 °C (larger particles), thus showing that their size depends on the activation conditions used. Similar spheres are observed in the original samples upon activation (Fig. S8). These nanospheres are typical in thermally treated biomass-based residues and could arise from polymerization of saccharides or polyphenols. Similar spherical micrometer-size nanoparticles were observed by Sevilla et al. upon hydrothermal carbonization of carbohydrates (glucose, sucrose and starch) (Sevilla et al., 2009). Fe, C and S mapping shows that these three elements are homogenously distributed in the evaluated regions. The similarity in size and shape between the spherical nanospheres (Figs. 4 and 5) and the core-shell nanoparticles observed with TEM (Fig. 1A) confirm that these outer nanospheres correspond indeed to the iron/graphite nanoparticles. Their homogeneous distribution confirms the success of the HTC process in the preparation of perfectly designed core-shell carbon-encapsulated iron nanoparticles. At this point it is important to highlight the larger size of these Fe@carbon nanospheres after a thermal treatment at 1000 °C (Fig. S8), also reflected in the iron XPS content described in Table S3, and in agreement with TEM images (Fig. 1A). Iron sintering at high temperatures could be one of the reasons to explain the poor performance of sample HC-OMW-1000 in the H_2S removal process.

To further understand the reaction process, original and used catalysts were evaluated using thermogravimetric analysis under a nitrogen atmosphere. The main goal was to identify differences in the surface evolved species before and after the H_2S experiments. Fig. 6 compares the TG profiles for the original and used catalysts in the temperature range from 25 °C to 1500 °C. As expected, the weight loss in all catalysts is much higher in the used samples due to the formation of sulfur-based species, the weight loss decreasing with the thermal background of the evaluated samples (600 °C > 800 °C > 1000 °C). Original samples exhibit three small weight losses at ca. 140 °C, 700 °C and 950 °C attributed to the decomposition of oxygen-containing functional groups (low temperature peak), and decomposition of deposited amorphous/defective carbon structures at high temperatures (Liu et al., 2007; Han et al., 2016). Han et al. proposed similar weight changes above 600 °C for GO, r-GO and graphite (Han et al., 2016). The higher stability of the surface species in samples HC-OMW-800 and HC-OMW-1000 must be attributed to the thermal history of these samples and the lower content of amorphous/defective carbon (higher graphitization degree).

Concerning the used catalysts, thermal analysis shows some differences compared to the original samples. All samples exhibit an initial weight loss at relatively low temperatures (275 °C–297 °C), not present in the fresh catalysts. This peak is relatively large (main component) for samples HC-OMW-600 and HC-OMW-800, i.e., the most active catalysts. Bandosz et al. observed similar decomposition peaks in activated carbon materials after serving as H_2S adsorbents, and attributed them to the vaporization of surface generated species, mainly sulfur, or the decomposition (or oxidation when using air in the TG) of adsorbed sulfuric and sulfurous acids (with the associated emission of SO_3 and SO_2) (Bandosz et al., 2002, Bandosz et al., 1999). Vaporization of elemental sulfur can explain these low-temperature peaks, taking into account the large

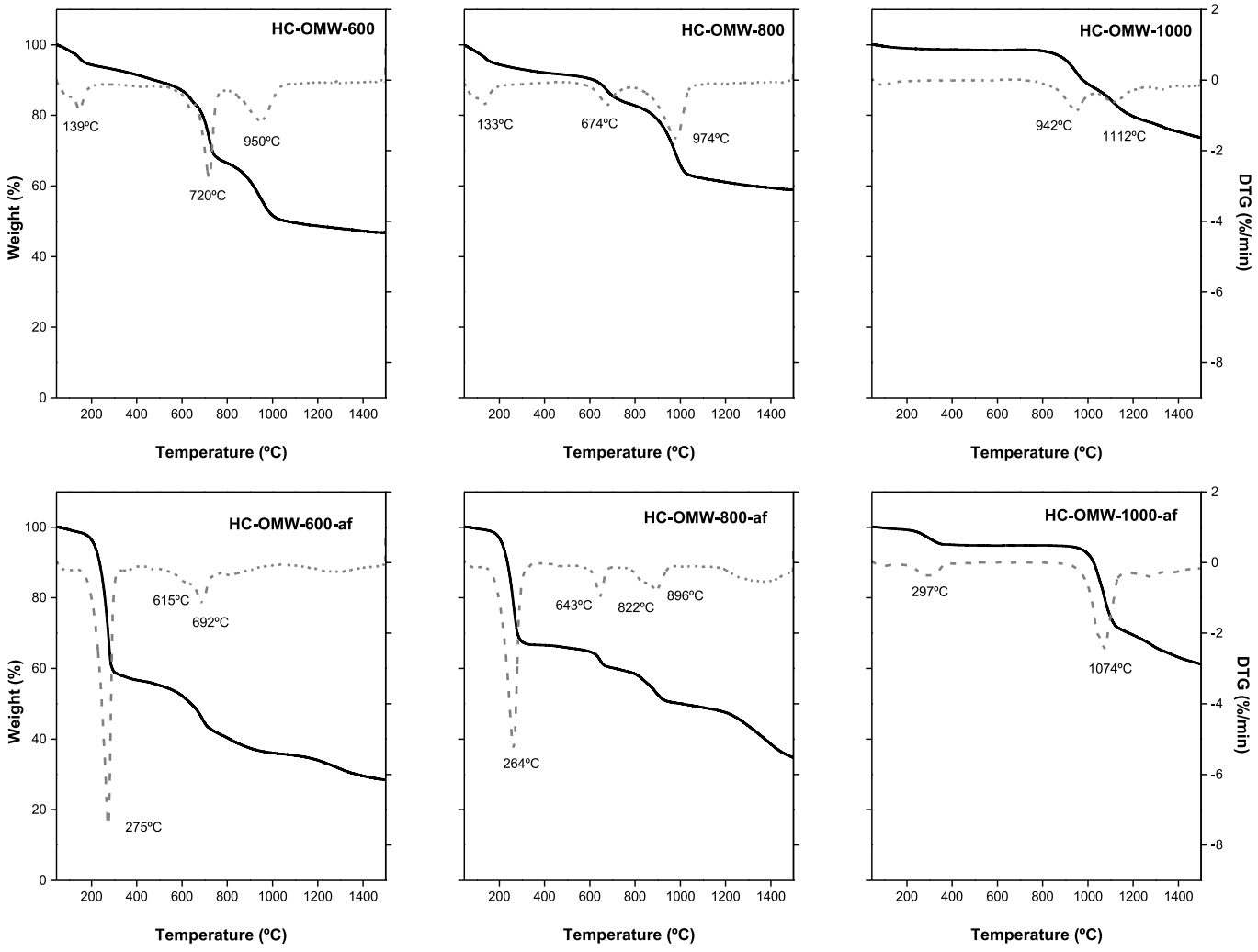

Fig. 6. Thermogravimetric analysis of the three evaluated catalysts original and used in the H_2S breakthrough column experiments.

content of elemental sulfur identified using XPS in the used HC-OMW-T catalysts. TG profiles of the used catalysts show additional peaks in the temperature range 600 °C–1000 °C, most probably due to the decomposition of other sulfur species associated with the graphite microdomains (most probably due to newly created polysulfide species C–S–S–S–C in surface carbon defects).

3.4. Comparison with commercial catalysts

To identify the potential of the HC-OMW-T catalysts in the conversion of H_2S, similar experiments were performed using two dedicated catalysts for H_2S developed and commercialized by Jacovi Group Ltd. Fig. S9 compares the breakthrough column test for samples ADDSORB™ VA3 (coal-based sample impregnated with KOH) and ADDSORB™ VA6 (impregnated activated carbon). VA adsorbents are commercialized as one of the most promising systems for the removal of acid gases in industrial streams (containing oxygen and humidity). Breakthrough tests show the typical profile for acid-base adsorbents with a sharp increase in H_2S concentration after the break point with a total removal capacity of 177 and 204 mg/g, for samples ADDSORB™ VA6 and ADDSORB™ VA3, respectively. The results obtained with the HC-OMW-based samples constitute more than a three-fold increase in the adsorption/oxidation capacity compared to these commercial samples. Similar experiments described in the literature using iron hydroxides (e.g., α-FeOOH) supported on activated carbon powder reported a total capacity of 171 mg/g, a large improvement compared to the non-supported iron hydroxide (46 mg/g) (Lee et al., 2017). Bulk oxides/hydroxides suffer from sintering processes with the associated reduction in the active surface and the oxidation capacity (Lian et al., 2009). Dispersion of these active phases in carbon materials has been widely applied as a promising approach to improve the catalytic performance, although with limited removal performance (Choudhury and Lansing, 2021; Lee et al., 2017; Zeng et al., 2015). Based on these premises, application of hydrothermal synthesis (HTC) using biomass-based residues can be envisaged as a highly promising approach to reach high iron contents, with a high dispersion, with minimal aggregation, and to provide an optimum in the exposed active sites. Our finding constitutes a step-stone towards industrial application of these encapsulated Fe@carbon nanoparticles for the efficient removal of H_2S in industrial streams at room temperature.

4. Conclusions

Fe@carbon-rich nanoparticles have been successfully prepared from an industrial waste (oil mill wastewater-OMW) using catalyzed hydrothermal carbonization. Upon a thermal processing at high temperatures (above 800 °C), these hybrid nanoparticles are converted into nanostructured architectures with a core-shell morphology. More specifically, amorphous carbon deposits are converted into highly ordered graphite microdomains encapsulating the α-Fe/Fe_3O_4 nanoparticles. Thermal processing also promotes the development of micro-/mesoporosity and the aromatization of the graphite layers. Once characterized, these hybrid nanoparticles have been tested in the removal of H_2S at room temperature. Experimental results demonstrate the exceptional performance of these HC-OMW-T catalysts, preferentially under oxygen-rich conditions and in the presence of moisture. The total removal capacity of these samples after three days reaches more than 0.5–0.6 g/g, a three-fold increase compared to dedicated commercial adsorbents. Post-mortem characterization of the used catalysts anticipates the preferential formation of elemental sulfur deposits and polysulfide anions, most probably associated with the defective graphite microdomains.

CRediT authorship contribution statement

M. Abid: Investigation, Formal analysis, Data curation. **R. Garcia:** Investigation, Formal analysis. **M. Martinez-Escandell:** Conceptualization. **A. Fullana:** Writing – review & editing, Supervision, Methodology. **J. Silvestre-Albero:** Writing – review & editing, Writing – original draft, Supervision, Project administration, Conceptualization.

Declaration of competing interest

The authors declare that they have no known competing financial interests or personal relationships that could have appeared to influence the work reported in this paper.

Data availability

Data will be made available on request.

Acknowledgment

J.S.A acknowledges financial support from MCIN/AEI/10.13039/501100011033 and EU NextGeneration/PRTR (Project PCI2020-111968/3D-Photocat), MCIN (Project PID2022-142960OB-C21) and Conselleria de Innovación, Universidades, Ciencia y Sociedad Digital, Generalitat Valenciana (Project CIPROM/2021/022). M.A. acknowledges financial support from the Algerian Ministry of Higher Education and Scientific Research.

Appendix A. Supplementary data

Supplementary data to this article can be found online at https://doi.org/10.1016/j.chemosphere.2024.142140.

References

Abdullah, H., Ramli, I., Ismail, I., Yusof, N.A., 2017. Hydrocarbon sources for the carbon nanotubes production by chemical vapour deposition: a review. Pertanika J. Sci. Technol. 25, 379–396.

Bagreev, A., Bandosz, T.J., 2022. A role of sodium hydroxide in the process of hydrogen sulfide adsorption/oxidation on caustic-impregnated activated carbons. Ind. Eng. Chem. Res. 41, 672–679. https://doi.org/10.1021/ie010599r.

Balsamo, M., Cimino, S., de Falco, G., Erto, A., Lisi, L., 2016. ZnO-CuO supported on activated carbon for H_2S removal at room temperature. Chem. Eng. J. 304, 399–407. https://doi.org/10.1016/j.cej.2016.06.085.

Bandosz, T.J., 1999. Effect of pore structure and surface chemistry of virgin activated carbons on removal of hydrogen sulfide. Carbon 37, 483–491. https://doi.org/10.1016/S0008-6223(98)00217-6.

Bandosz, T.J., 2002. On the adsorption/oxidation of hydrogen sulfide on activated carbons at ambient temperatures. J. Colloid Interface Sci. 246, 1–20. https://doi.org/10.1006/jcis.2001.7952.

Bandosz, T.J., Bagreev, A., Adib, F., Turk, A., 1999. Unmodified versus caustic-impregnated carbons for control of hydrogen sulfide emissions from sewage treatment plants. Environ. Sci. Technol. 34, 1069–1074. https://doi.org/10.1021/es9813212.

Calderón, B., Smith, F., Aracil, I., Fullana, A., 2018. Green synthesis of thin shell carbon-encapsulated nanoparticles via hydrothermal carbonization. ACS Sustainable Chem. Eng. 6, 7995–8002. https://doi.org/10.1021/acssuschemeng.8b01416.

Chen, Y., Ma, C., Wu, Y., Ke, C., Liu, X., Wang, J., Qiao, W., Ling, L., 2022. Efficient removal of H2S with zinc oxide/nitrogen-doped ordered mesoporous carbons at room temperature. Microporous Mesoporous Mater. 333, 111712 https://doi.org/10.1016/j.micromeso.2022.111712.

Choudhury, A., Lansing, S., 2021. Adsorption of hydrogen sulfide in biogas using a novel iron-impregnated biochar scrubbing system. J. Environ. Chem. Eng. 9, 104837 https://doi.org/10.1016/j.jece.2020.104837.

Cuesta, A., Dhamelincourt, P., Laureyns, J., Martínez-Alonso, A., Tascón, J.M.D., 1994. Raman microprobe studies on carbon materials. Carbon 32, 1523–1532. https://doi.org/10.1016/0008-6223(94)90148-1.

Davydov, A., Chuang, K.T., Sanger, A.R., 1998. Mechanism of H2S oxidation by ferric oxide and hydroxide surfaces. J. Phys. Chem. B 102, 4745–4752. https://doi.org/10.1021/jp980361p.

Ferrari, A.C., Meyer, J.C., Scardaci, V., Casiraghi, C., Lazzeri, M., Mauri, F., Piscanec, S., Jiang, D., Novoselov, K.S., Roth, S., Geim, A.K., 2006. Raman spectrum of graphene and graphene layers. PRL 97, 187401. https://doi.org/10.1103/PhysRevLett.97.187401.

Gore, J.P., Sane, A., 2011. Flame synthesis of carbon nanotubes. In: Yellampalli, S. (Ed.), Carbon Nanotubes Synthesis, Characterization, Applications. Intech Open. https://doi.org/10.5772/21012.

Han, H., Jiang, C., Huo, L., Gao, J., 2016. Mechanical and thermal properties of cationic ring-opening o-cresol formaldehyde epoxy/polyurethane acrylate composites enhanced by reducing graphene oxide. Polym. Bull. 73, 2227–2244. https://doi.org/10.1007/s00289-016-1605-7.

Kaliva, A.N., Smith, J.W., 1983. Oxidation of low concentrations of hydrogen sulfide by air on a fixed activated carbon bed. Can. J. Chem. Eng. 61, 208–212. https://doi.org/10.1002/cjce.5450610210.

Lang, Y., Butler, E.C., 2016. Iron-sulfide-associated products formed during reductive dechlorination of carbon tetrachloride. Environ. Sci. Technol. 50, 5489–5497. https://doi.org/10.1021/acs.est.5b06154.

Lee, S., Lee, T., Kim, D., 2017. Adsorption of hydrogen sulfide from gas streams using the amorphous composite of α-FeOOH and activated carbon powder. Ind. Eng. Chem. Res. 56, 3116–3122. https://doi.org/10.1021/acs.iecr.6b04747.

Li, L., Ma, P., Hussain, S., Jia, L., Lin, D., Yin, X., Lin, Y., Cheng, Z., Wang, L., 2019. FeS_2/carbon hybrids on carbon cloth: a highly efficient and stable counter electrode for dye-sensitized solar cell. Sustain. Energy Fuels 3, 1749–1756. https://doi.org/10.1039/C9SE00240E.

Lian, J., Duan, X., Ma, J., Peng, P., Kim, T., Zheng, W., 2009. Hematite (α-Fe_2O_3) with various morphologies: ionic liquid-assisted synthesis, formation mechanism and properties. ACS Nano 3, 3749–3761. https://doi.org/10.1021/nn900941e.

Liu, B.S., Jiang, L., Sun, H., Au, C.T., 2007. XPS, XAES, and TG/DTA characterization of deposited carbon in methane dehydroaromatization over Ga-Mo/ZSM-5 catalysts. Appl. Surf. Sci. 253, 5092–5100. https://doi.org/10.1016/j.apsusc.2006.11.031.

Liu, D., Li, B., Wu, J., Liu, Y., 2020. Sorbents for hydrogen sulfide capture from biogas at low temperature: a review. Environ. Chem. Lett. 18, 113–118. https://doi.org/10.1007/s10311-019-00925-6.

Mikhlin, Y., Romanchenko, A., Tomashevich, Y., 2001. Surface and interface analysis of iron sulfides in aqueous media using photoelectron spectroscopy of fast-frozen dispersions. Appl. Surf. Sci. 549, 149261 https://doi.org/10.1016/j.apsusc.2021.149261.

Muñoz, M., Nieto-Sandoval, J., Alvarez-Torrellas, S., Sanz-Santos, E., Calderon, B., de Pedro, Z.M., Larriba, M., Fullana, A., García, J., Casas, J.A., 2021. Carbon-encapsulated iron nanoparticles as reusable adsorbents for micropollutants removal from water. Sep. Purif. Technol. 257, 117974 https://doi.org/10.1016/j.seppur.2020.117974.

Pudi, A., Rezaei, M., Signorini, V., Andersson, M.P., Baschetti, M.G., Mansouri, S.S., 2022. Hydrogen sulfide capture and removal technologies: a comprehensive review of recent developments and emerging trends. Sep. Purif. Technol. 298, 121448 https://doi.org/10.1016/j.seppur.2022.121448.

Qian, H.-S., Yu, S.-H., Luo, L.-B., Gong, J.-Y., Fei, L.-F., Liu, X.-M., 2006. Synthesis of uniform Te@carbon-rich composite nanocables with photoluminescence properties and carbonaceous nanofibers by the hydrothermal carbonization of glucose. Chem. Mater. 18, 2102–2108. https://doi.org/10.1021/cm052848y.

Sevilla, M., Fuertes, A.B., 2009. Chemical and structural properties of carbonaceous products obtained by hydrothermal carbonization of saccharides. Chem. Eur J. 15, 4195–4203. https://doi.org/10.1002/chem.200802097.

Shang, G., Shen, G., Liu, L., Chen, Q., Xu, Z., 2013. Kinetics and mechanisms of hydrogen sulfide adsorption by biochars. Bioresour. Technol. 133, 495–499. https://doi.org/10.1016/j.biortech.2013.01.114.

Shi, N., Liu, Q., He, X., Wang, G., Chen, N., Peng, J., Ma, L., 2019. Molecular structure and formation mechanism of hydrochar from hydrothermal carbonization of carbohydrates. Energy Fuel. 33, 9904–9915. https://doi.org/10.1021/acs.energyfuels.9b02174.

Sun, Y., Zhang, X., Zhang, M., Ge, M., Wang, J., Tang, Y., Zhang, Y., Mi, J., Cai, W., Lai, Y., Feng, Y., 2022. Rational design of electrospun nanofibers for gas purification: principles, opportunities, and challenges. Chem. Eng. J. 446, 137099 https://doi.org/10.1016/j.cej.2022.137099.

Thommes, M., Kaneko, K., Neimark, A.V., Olivier, J.P., Rodriguez-Reinoso, F., Rouquerol, J., Sing, K.S.W., 2015. Physisorption of gases, with special reference to the evaluation of surface area and pore size distribution (IUPAC Technical Report). Pure Appl. Chem. 87, 1051–1069. https://doi.org/10.1515/pac-2014-1117.

Tian, Z., Wang, C., Yue, J., Zhang, X., Ma, L., 2019. Effect of potassium promoter on the Fischer-Tropsch synthesis of light olefins over iron carbide catalysts encapsulated in graphene-like carbon. Catal. Sci. Technol. 9, 2728–2741. https://doi.org/10.1039/C9CY00403C.

van Zandvoort, I., Koers, E.J., Weingarth, M., Bruijnincx, P.C.A., Baldus, M., Weckhuysen, B.M., 2015. Structural characterization of 13C-enriched humins and alkali-treated ^{13}C humins by 2D solid-state NMR. Green Chem. 17, 4383–4392. https://doi.org/10.1039/C5GC00327J.

Vargas-Estrada, L., Hoyos, E.G., Mendez, L., Sebastian, P.J., Muñoz, R., 2023. Boosting photosynthetic biogas upgrading via carbon-coated zero-valent nanoparticle addition: a pilot proof of concept study. Sustain. Chem. Pharm. 31, 100952 https://doi.org/10.1016/j.scp.2022.100952.

Wang, L., Chen, T., Liu, H., Li, W., Zou, X., Wang, C., Li, M., 2019. Comprehensive application of Oolitic hematite for H2S removal at high temperature: performance and mechanism. Energy Fuel 33, 2037–2044. https://doi.org/10.1021/acs.energyfuels.8b04261.

Wei, S., Li, Z., Sun, Y., Zhang, J., Ge, Y., Li, Z., 2022. A comprehensive review on biomass humification: recent advances in pathway challenges, new applications, and perspectives. Renewable Sustainable Energy Rev. 170, 112984 https://doi.org/10.1016/j.rser.2022.112984.

Yang, S., Song, X., Zhang, P., Sun, J., Gao, L., 2014. Self-assembled α-Fe_2O_3 mesocrystals/graphene nanohybrid for enhanced electrochemical capacitors. Small 10, 2270–2279. https://doi.org/10.1002/smll.201303922.

Yu, S.-H., Cui, X., Li, L., Li, K., Yu, B., Antonietti, M., Cölfen, H., 2004. From starch to metal/carbon hybrid nanostructures: hydrothermal metal-catalyzed carbonization. Adv. Mater. 16, 1636–1640. https://doi.org/10.1002/adma.200400522.

Zeng, Y., Zeng, Z., Ju, T., Zhang, F., 2015. Adsorption performance and mechanism of perchloroethylene on a novel nano composite β-FeOOH-AC. Microp. Mesop. Materials 210, 60–68. https://doi.org/10.1016/j.micromeso.2015.02.021.

Zhang, C., Deng, L., Zhang, P., Ren, X., Li, Y., He, T., 2017. Electrospun FeS nanorods with enhanced stability as counter electrodes for dye-sensitized solar cells. Electrochim. Acta 229, 229–238. https://doi.org/10.1016/j.electacta.2017.01.148.